ISSN 1560-3547, Regular and Chaotic Dynamics, 0000, Vol. 00, No. 0, pp. 1–11. © RCD Editorial Office, 2016.

arXiv:2011.04042v1 [physics.chem-ph] 8 Nov 2020

Dynamics and bifurcations on the normally hyperbolic invariant manifold of a periodically driven system with rank-1 saddle

Manuel Kuchelmeister[1], Johannes Reiff[1], Jörg Main[1], and Rigoberto Hernandez[2,3*]

[1] *Institut für Theoretische Physik I, Universität Stuttgart, 70550 Stuttgart, Germany*

[2] *Department of Chemistry, Johns Hopkins University, Baltimore, Maryland 21218, United States*

[3] *Departments of Chemical & Biomolecular Engineering, and Materials Science and Engineering, Johns Hopkins University, Baltimore, Maryland 21218, United States*

Received July 12, 2020; accepted September 09, 2020

Abstract—In chemical reactions, trajectories typically turn from reactants to products when crossing a dividing surface close to the normally hyperbolic invariant manifold (NHIM) given by the intersection of the stable and unstable manifolds of a rank-1 saddle. Trajectories started exactly on the NHIM in principle never leave this manifold when propagated forward or backward in time. This still holds for driven systems when the NHIM itself becomes time dependent. We investigate the dynamics on the NHIM for a periodically driven model system with two degrees of freedom by numerically stabilizing the motion. Using Poincaré surfaces of section we demonstrate the occurrence of structural changes of the dynamics, *viz.*, bifurcations of periodic transition state (TS) trajectories when changing the amplitude and frequency of the external driving. In particular, periodic TS trajectories with the same period as the external driving but significantly different parameters—such as mean energy—compared to the ordinary TS trajectory can be created in a saddle-node bifurcation.

MSC2010 numbers: 37D05, 37G15, 37J20, 37M05, 65P30

DOI: 10.0000/S1560354700000012

Keywords: *transition state theory, rank-1 saddle, normally hyperbolic invariant manifold, stroboscopic map, bifurcation*

1. INTRODUCTION

Transition state theory (TST) [1–18] is well established for the computation of rates in systems with a rank-1 saddle. In these systems, two different states—*viz.*, reactants and products—are classified and separated by an appropriately chosen dividing surface (DS). TST uses the flux through the DS to determine the rate of a chemical reaction or a similar process. It has been applied in a broad range of problems in a broad range of fields including atomic physics [19], solid state physics [20], cluster formation [21, 22], diffusion dynamics [23, 24], cosmology [25], celestial mechanics [26, 27], and Bose-Einstein condensates [28–32]. For systems, which are time-dependently driven—e.g., by an oscillating external field—the situation becomes more challenging because the DS itself becomes time dependent and depends non-trivially on the moving saddle of the potential [33, 34]. The DS can nevertheless be obtained by time-dependent perturbation theory [35], through a minimization procedure based on a Lagrangian descriptor [36–39], and other approaches [39, 40]. Addressing such perturbations is particularly relevant to the use of chemical control through external fields [41–46].

In a system with d degrees of freedom, the time-dependent DS embedded in phase space has dimension $2d-1$. It is attached to a $(2d-2)$-dimensional normally hyperbolic invariant manifold

*Correspondence to: r.hernandez@jhu.edu

(NHIM), which has the property that every particle on the NHIM will never leave this manifold when propagated forward or backward in time. The importance of the geometric structure—with respect to bifurcations and other objects—of the NHIM on dynamical systems without driving has been understood for some time [47] and continues to receive attention [48–50]. The bifurcation of the periodic orbit dividing surface (PODS) in two degrees of freedom (DoFs) upon varying the total energy was revealed by Pechukas, Pollak, and Child [51–53]. Li *et al.* [54] extended their work to three DoFs showing that the invariants of motion of the bath modes can be used to control the bifurcation of the NHIM. In general, bifurcations of the NHIM give rise to its breakdown leading to switching between the dominant reaction coordinate as a function of total energy of the system [55, 56], and further leads to the possibility of experimental control [57]. In this work, we investigate the degree to which such control can play a role in driven systems.

In periodically driven systems with only one degree of freedom, the NHIM reduces to a point that oscillates with the same period as the driving potential [33, 34, 58–65]. This periodic orbit is the one-dimensional transition state (TS) trajectory. In systems with two or more degrees of freedom, the structure of the NHIM and the dynamics of trajectories on it becomes non-trivial. Slowly reacting particles spend a longer time in the vicinity of the NHIM crossing the DS closer to the NHIM, and therefore the dynamics on the NHIM is of special interest [66].

In this paper, we resolve the dynamics on the NHIM of a periodically driven two-dimensional system. We find that the structural changes in the dynamics are sensitive to variations in the amplitude and frequency of the external driving. Using the tools of dynamical systems theory, we can resolve the stable structures arising from periodic orbits and visible as tori in the Poincaré surface of section (PSOS). With increasing perturbation through external driving, we find bifurcations that signal emergent behavior inside of the NHIM.

2. THEORY AND METHODS

A pair of fundamental assumptions in the original construction of TST is that chemical reaction kinetics can be modeled by nuclear motion on a Born-Oppenheimer surface, and that said motion can be described by classical mechanics. The system can be represented as a multidimensional effective particle. Its evolution is a trajectory on the potential energy surface connecting reactant and product regions or valleys. In a typical scenario, there exists a rank-1 saddle between these regions. The third of TST's assumption is that there exists a DS associated somehow with this TS[1)] whose associated directional flux weighted by the (reactant) population is a rate constant. This connection is exact only if the DS is recrossing-free. Below, we review the geometric approaches that have been developed to construct it. An additional layer of complexity arises when the system is driven by time-dependent potentials [15]. A recent method for the construction of the associated time-dependent DS in 1-DoF is also discussed below. Together, this section sets the stage for the elaboration of these methods in the context of the 2-DoF system that form the central results presented in the next section.

2.1. Model system

For the investigation of the dynamics on the NHIM and the dependence of the dynamics on parameters of the external driving, we use a two-dimensional model system which has already been studied in previous publications [39, 67, 68]. The time-dependent potential

$$V(x,y,t) = 2\exp\{-[x-\hat{x}\sin(\omega_x t)]^2\} + 2\left[y - \frac{2}{\pi}\arctan(2x)\right]^2 \tag{2.1}$$

describes a two-dimensional, periodically oscillating energy landscape including a rank-1 saddle. The saddle's unstable direction is constructed via a Gaussian barrier along the approximate *reaction coordinate* x. To make the saddle time-dependent, the barrier's position is driven time-periodically. Both the driving amplitude $\hat{x}$ and frequency ω_x will be varied in the following sections. In order to expand the system to two DoFs, a harmonic oscillator is added through an *orthogonal mode* y.

[1)] Note that we use the phrase *transition state* to refer to the ensemble of states bound indefinitely to the saddle region, i. e., those located on the codimension-2 NHIM. This is distinct from the codimension-1 *dividing surface*. See footnote 6 of Ref. [14] for a more detailed discussion.

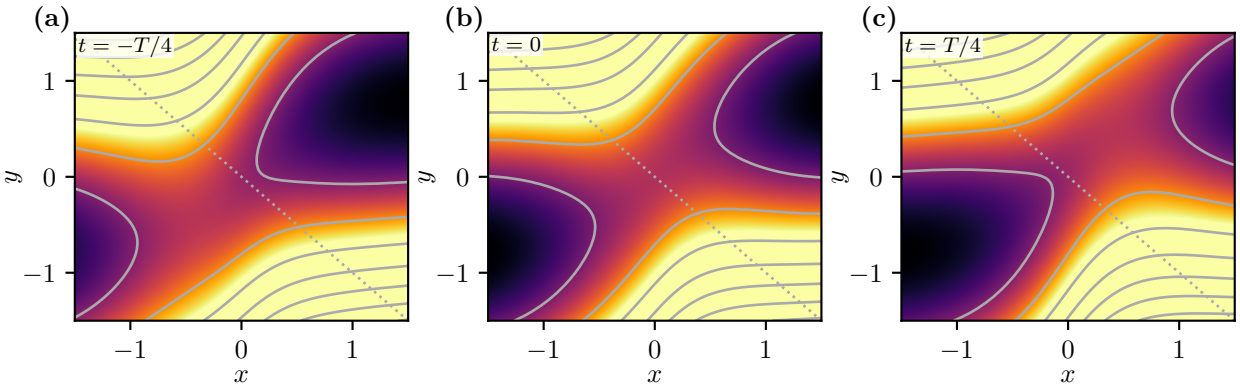


Fig. 1. Time-dependent potential $V(x, y, t)$ of the model described by Eq. (2.1) with $\hat{x} = 0.4$ and $\omega_x = 2\pi/T$ at three different times t given in the figures. The dotted diagonal line serves as a guide to the eye.

This new DoF is coupled via the nonlinear term $\arctan(2x)$, resulting in non-separable dynamics in the vicinity of the reaction without changing the properties on the reactant and product regions. Further system parameters, such as the strength of the harmonic oscillator or the saddle height and width, are not changed throughout this paper and are therefore set to fixed values. This prototypical potential, which can be used to describe chemical reactions qualitatively, is depicted in Fig. 1 at three different points in time t. In the following we investigate the dynamics on the NHIM parameterized by the orthogonal modes y, v_y, and time t.

2.2. Basics of transition state theory

We begin by considering the time-invariant case of a reactive 1-DoF system with an energy barrier along the reaction coordinate x separating reactants from products. Depending on the initial conditions and therefore the energy, most particles can be classified as either 1) non-reactive reactants, 2) non-reactive products, 3) reactive reactants, or 4) reactive products. This results in four distinct regions in phase space, as indicated in Fig. 2. Trajectories started at initial conditions within any of these regions eventually leave the barrier's vicinity both forward and backward in time.

The regions are separated by two kinds of critical trajectories. The points initiating trajectories that approach the barrier top without reaching it as $t \to \infty$ and leave its vicinity when propagating backward in time form the stable manifold $\mathcal{W}_\mathrm{s}$; the reverse is called the unstable manifold $\mathcal{W}_\mathrm{u}$. Both manifolds belong to a hyperbolic fixed point at their closures' intersection called the NHIM. In the special case of a time-invariant 1-DoF Hamiltonian, the NHIM is associated with the unstable trajectory for which a particle remains precariously fixed at the barrier maximum. Such a trajectory is an example of the TS trajectory. We can extend this structure to periodically driven systems. Now, the NHIM—or TS trajectory—will be time-dependent as well, but it detaches from the barrier's maximum. Its defining property—a set of unstable trajectories trapped indefinitely in the vicinity of the barrier—still applies.

To numerically resolve the reactive and nonreactive regions presented above, one has to determine in which state—reactant or product—particles start from, and in which state they end. This can be defined through the use of an interaction region—namely an interval along the reaction coordinate x—outside of which the system is *clearly* in the reactant or product regions. One can then associate initial conditions to one of the regions by propagating the corresponding particle both forward and backward in time until it leaves the interaction region to the reactant or product side.

This classification can be used to precisely calculate the position of the stable and unstable manifolds as well as the NHIM. For the former, a bisection algorithm which finds the border between two adjacent regions can be employed. Since these borders meet at a hyperbolic fixed point, the NHIM's position can be determined by linking the four bisections belonging to the stable and unstable manifolds. The resulting algorithm is called the binary contraction method (BCM) [40] and is illustrated in Fig. 2. This conjectured algorithm has been seen to result in a NHIM in all of the chemically-motivated applications we have employed it. This is however not guaranteed to

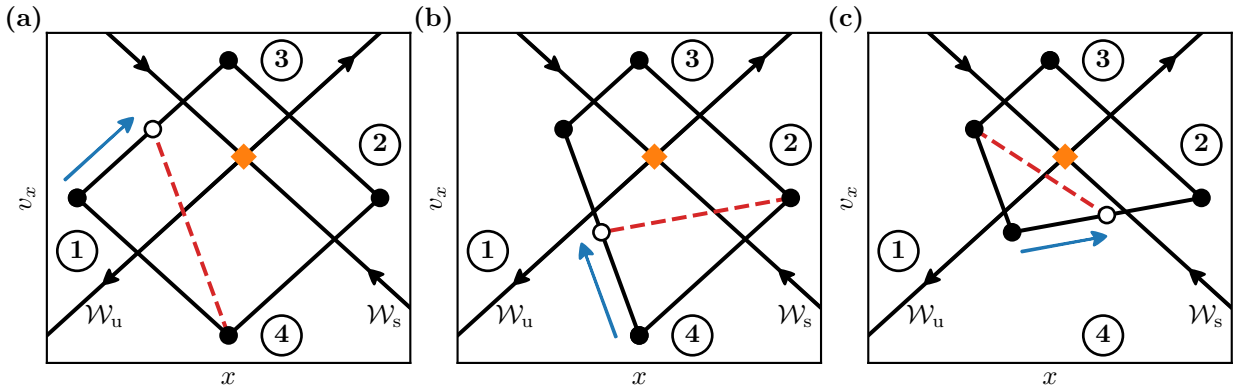


Fig. 2. Use of the binary contraction method to uncover the NHIM in phase space. The stable $\mathcal{W}_\mathrm{s}$ and unstable $\mathcal{W}_\mathrm{u}$ manifolds associated with the barrier divide the phase space into distinct regions labeled 1 through 4. The NHIM is located at the intersection of the two manifolds' closures and is marked with a diamond. To numerically obtain this point, a quadrangle with one corner in each region is set up. In turn, the midpoint for every edge is determined, shown as an empty circle. Depending on which region the midpoint is in, it subsequently replaces one of the previous corners. This procedure is repeated until the quadrangle is sufficiently small. Frames a, b, and c show the first three steps of the method.

converge in diabolical cases characterized by multiple saddles in proximity, although it did work if they were sufficiently far apart [69].

The simple picture presented above can be extended to systems with arbitrarily many DoFs. The potential energy landscape in a d-DoF system typically features a rank-1 saddle separating reactants from products. While there is still a single unstable reaction coordinate x, we now have $d-1$ additional stable orthogonal modes $\boldsymbol{y}$. As a consequence, the stable and unstable manifolds become hypersurfaces with codimension 1 in phase space. Similarly, the NHIM becomes a codimension 2 manifold located at the intersection of the closures of $\mathcal{W}_\mathrm{s}$ and $\mathcal{W}_\mathrm{u}$. Likewise, the TS describes the ensemble of all trajectories confined to the NHIM. If coordinates are chosen well, every x–v_x section of the phase space for a given position $\boldsymbol{y}$ and velocity $\boldsymbol{v}_y$ shows the cross-like structure shown in Fig. 2. The numerical algorithms presented above can therefore be used without modification to calculate individual points of the NHIM.

2.3. Dynamics on the NHIM

The aim of this paper is to uncover and resolve non-trivial structures and dynamics on the NHIM as revealed below. Unfortunately, in the case of a 1-DoF system, the dynamics on the NHIM is trivial since it only consists of one point. This single point does not have an internal structure. If the system is time-invariant, even a 2-DoF system exhibits integrable dynamics on the NHIM because the effective dynamics is one dimensional and the energy is conserved. In the following, we therefore investigate a time-dependent 2-DoF system as it is large enough to exhibit nontrivial behavior, but small enough to be visualized.

Despite the fact that the NHIM is a mathematically invariant subspace, trajectories started on it deviate exponentially fast as time goes by because of limited numerical precision. Therefore, numerically calculated trajectories have to be stabilized explicitly on the NHIM, e. g. using the BCM. Therein, after each time step Δt, the coordinates x and v_x are recalculated to project the particle back onto the NHIM. A similar projection has been used in Ref. [68]. Care has to be taken to ensure that this projection does not introduce significant errors. To achieve this, the projected distance in x and v_x is measured. If a maximum distance is exceeded, the projection is rejected and the particle is reset to an earlier time and position. The propagation is then repeated with a smaller value of Δt. In the present case, an empirical maximum distance of $\sqrt{(\Delta x)^2 + (\Delta v_x)^2} \leq 10^{-3}$ has been used. We found numerically that smaller thresholds do not change the results in a significant way, but we have yet to prove a rigorous bound on this threshold. This procedure effectively reduces the dimensionality on the subspace traversed by the trajectories from the four dimensions of the full phase space to the two dimensions of the NHIM. In higher dimensions, one could instead take advantage of an artificial neural net as recently done in Ref. [68] to stabilize the trajectories at the price of some loss in accuracy.

2.3.1. Poincaré surfaces of section

Although the NHIM in the present case is only a two-dimensional subspace, visualizing many trajectories on it can still get confusing quickly. A reliable method for such a task is the Poincaré map, also known as the PSOSs [70]. Using this method, the dimensionality of the phase space is reduced by only showing intersection points with a given sectional surface instead of the whole trajectory. When the system has a natural period, such as in the present case of a periodically driven system, one can effect a similar dimensional reduction using a stroboscopic map capturing periodic sections at corresponding intervals in time. For a time-dependent, effectively two-dimensional system, the stroboscopic PSOS corresponds to a set Σ given by

$$\Sigma = \left\{ \boldsymbol{\gamma}(t_n) \in \mathbb{R}^2 \;\middle|\; t_n = t_0 + nT, n \in \mathbb{N}_0 \right\}, \tag{2.2}$$

where $\boldsymbol{\gamma}(t) = (y(t), v_y(t))^\mathsf{T}$ denotes the phase space vector of the system constrained to the NHIM and T is the period of the driving. The previously continuous trajectory thereby becomes discretized under the stroboscopic map. In the numerical results presented below, the fixed points of the map are found using the modified Powell method, `scipy.optimize.root(method='hybr')`, implemented in the Python package SciPy [71].

2.3.2. Regular and chaotic dynamics

Dynamical properties, such as the integrability of the system, can be determined with the stroboscopic map introduced in the previous section. Near integrability is revealed by the existence of torus-like structures in the system's PSOS. Changes in the system's parameters, can lead to a transition from near integrable to chaotic as revealed by the emergence of stochastic structure in the PSOS.

A periodic trajectory with the property

$$\boldsymbol{\gamma}_n = \boldsymbol{\gamma}_{n+1} \quad \text{where} \quad \boldsymbol{\gamma}_n \equiv \boldsymbol{\gamma}(t_0 + nT) \quad \text{and} \quad n \in \mathbb{N}_0 \tag{2.3}$$

manifests as a fixed point with period T in the PSOS. Fixed points with periodicity sT, where $s \in \mathbb{N}$, analogously fulfill $\boldsymbol{\gamma}_n = \boldsymbol{\gamma}_{n+s}$. They appear as s-cycles in the PSOS since the stroboscopic map records a point once per system period T. The difference $\boldsymbol{\gamma}_{n+1} - \boldsymbol{\gamma}_n$ is a vector whose length increases monotonically with distance from the fixed point within the fixed point's neighborhood. This can be exploited to find fixed points through a root search algorithm.

There are two kinds of fixed points that must be distinguished: Elliptic fixed points belong to stable periodic orbits. Trajectories that start in the vicinity of such an orbit stay in its vicinity indefinitely. In the PSOS, these show up as concentric, possibly deformed torus-like structures. Hyperbolic fixed points, on the other hand, correspond to unstable orbits. Trajectories started in their vicinity act as if they were being repelled by the fixed point, leading to hyperbola-shaped structures in the PSOS.

When varying a system's parameters, its dynamics can change qualitatively in so-called bifurcations. Local bifurcations are identifiable via the creation or annihilation of fixed points. Most important for this paper are saddle-node bifurcations in which a pair of an elliptic and a hyperbolic fixed point emerge or vanish. A typical path from regular to chaotic, non-integrable dynamics is via an infinite series of bifurcations.

3. RESULTS AND DISCUSSION

3.1. Dependence of the dynamics on the external driving parameters

We start with the driving parameters used in our recent work [39], $\omega_x = \pi$ and $\hat{x} = 0.4$. To construct the PSOS, a number of trajectories are started on a specified domain at $t_0 = 0$ and are propagated for 100 periods each. It turns out that a reasonable choice for this domain is the set of points on the v_y axis at $y = 0$ as that is enough to map the full subspace of the NHIM. That is, given y and v_y, there exits only one x and v_x which keep the phase-space point on the NHIM. Thus, the trajectories are fully specified for a given y, v_y, and t and the restriction of $y = 0$ does not lose any generality in the PSOSs shown in Fig. 3a.

In the stroboscopic map, we can see a simple structure with a single elliptic fixed point. The elliptical patterns around it indicate that the system's dynamics on the NHIM is regular and

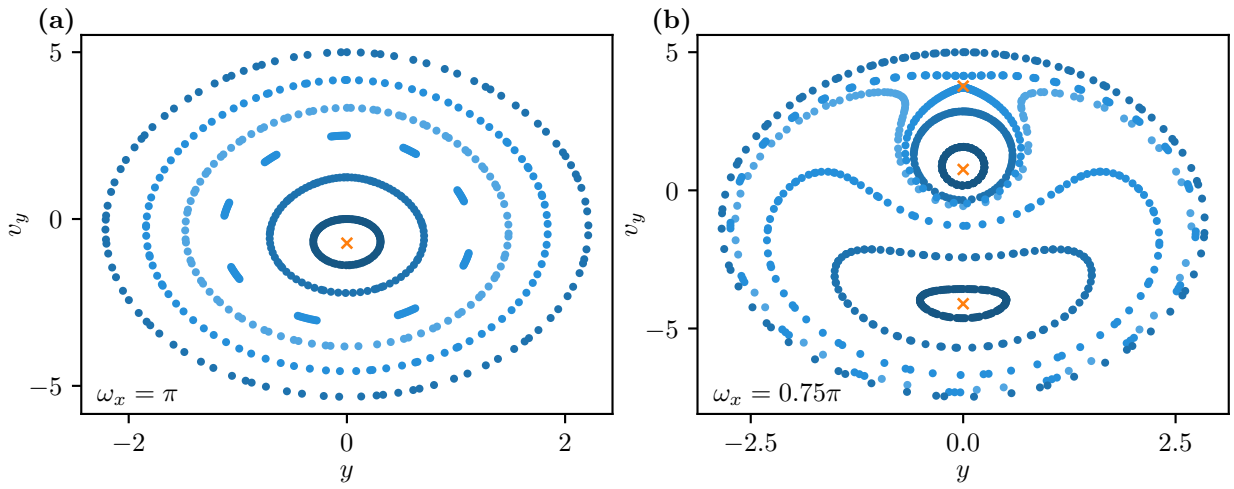


Fig. 3. Stroboscopic map of selected trajectories (PSOS) started at time $t_0 = 0$ for different frequencies ω_x. The driving amplitude is fixed at $\hat{x} = 0.4$. Crosses indicate fixed points. A color gradient is used to help distinguish neighboring trajectories. (a) With $\omega_x = \pi$, a single elliptic fixed point at $(y = 0, v_y \approx -0.72)$ exists. (b) When decreasing ω_x to 0.75π, this fixed point moves down to $v_y \approx -4.10$, while a pair of elliptic and hyperbolic fixed points emerge from a saddle-node bifurcation around $\omega_x \approx 0.802\pi$.

nearly integrable. Therefore, trajectories in phase space lie on two-dimensional tori, for which one approximate constant of motion exists [72]. In the neighborhood of the elliptic fixed point, resonance gaps can be seen, which indicates the existence of periodic orbits. Remaining trajectories are quasi-periodic, meaning they have an irrational winding number and that for arbitrary long integration times they would cover the entire torus surface area.

A qualitative change in the system's dynamics occurs in the PSOS when the frequency of driving is decreased to $\omega_x = 0.75\pi$, as can be seen in Fig. 3b: The elliptic fixed point from Fig. 3a moves down in v_y. In addition, a pair of fixed points—one elliptic and one hyperbolic—emerge from the saddle-node bifurcation as shown in Sec. 3.1.1. As a result, the elliptic structure of the original fixed point gets deformed significantly. While this changes its appearance, it does not lead to chaotic behavior.

3.1.1. Saddle-node bifurcations by variation of parameters

From Fig. 3, it seems natural to assume that there is a bifurcation in the parameter range $0.75\pi < \omega_x < \pi$. To confirm this assumption, we need to examine the fixed points systematically. To do so, fixed points were tracked using a root search algorithm as described in Sec. 2.3.2.

Figure 4 displays bifurcation diagrams, where the averaged total energy $\bar{E}_{\text{tot}}$ of trajectories associated with fixed points is shown as a function of saddle frequency ω_x and driving amplitude $\hat{x}$. In Fig. 4a, the driving frequency is varied between $0.71\pi \leq \omega_x \leq 0.85\pi$. One can clearly see the annihilation of a pair of fixed points—one elliptic and one hyperbolic—in a saddle-node bifurcation at $\omega_x \approx 0.802\pi$. For decreasing frequencies, the original elliptic fixed point from Fig. 3a gets pushed in the negative v_y direction away from the origin, while the new elliptic fixed point formed in the bifurcation slowly converges towards the origin. By contrast, the hyperbolic fixed point's position v_y increases for decreasing driving frequencies. Thus distinguishing the elliptic fixed point near the origin for slow and high driving frequencies must be done with some care.

Bifurcations do not only occur when changing the saddle's frequency, but also when altering its driving amplitude. This can be seen in Fig. 4b. The saddle frequency was set to $\omega_x = 0.8\pi$, near the parameter where the bifurcation occurs in Fig. 4a. Changing the saddle amplitude from $0 < \hat{x} \leq 1.47$ results in two saddle-node bifurcations, one annihilating a fixed point pair at $\hat{x} \approx 0.47$ and one creating a fixed point pair at $\hat{x} \approx 0.65$.

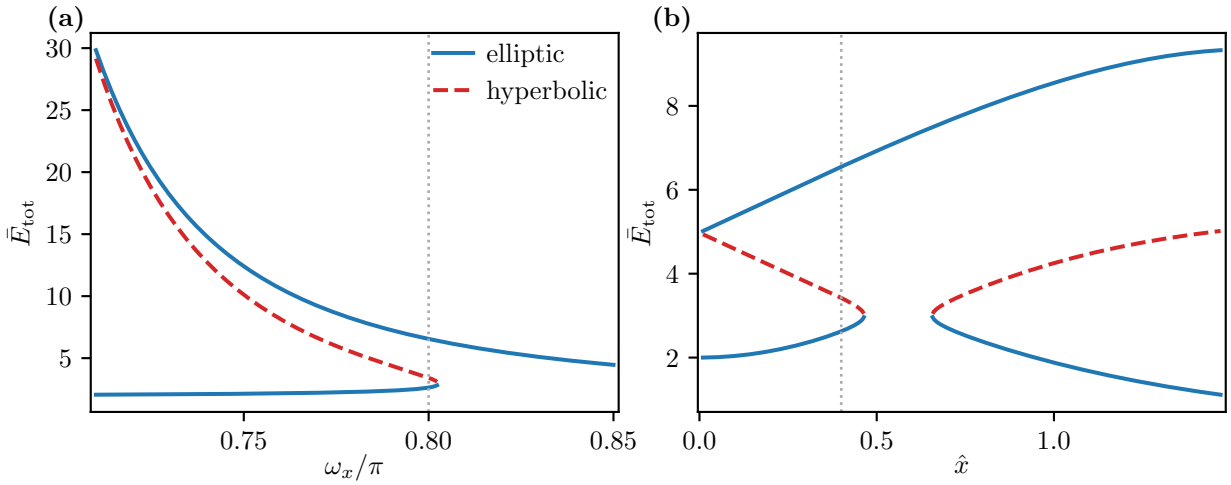


Fig. 4. (a) Average total energy $\bar{E}_{\mathrm{tot}}$ of periodic trajectories associated with fixed points (cf. Fig. 3) as a function of driving frequency ω_x. The driving amplitude is fixed at $\hat{x} = 0.4$. Around $\omega_x \approx 0.802\pi$, a pair of elliptic and hyperbolic fixed points annihilate in a saddle-node bifurcation. (b) Average total energy $\bar{E}_{\mathrm{tot}}$ analogous to (a) as a function of driving amplitude $\hat{x}$ for $\omega_x = 0.8\pi$. The system exhibits two saddle-node bifurcations around $\hat{x} \approx 0.47$ and $\hat{x} \approx 0.65$. At $\hat{x} = 0$, two orbits have identical potential energies and reversed velocities. Their total energies are therefore degenerate. Vertical lines indicate where the parameters of (a) and (b) intersect.

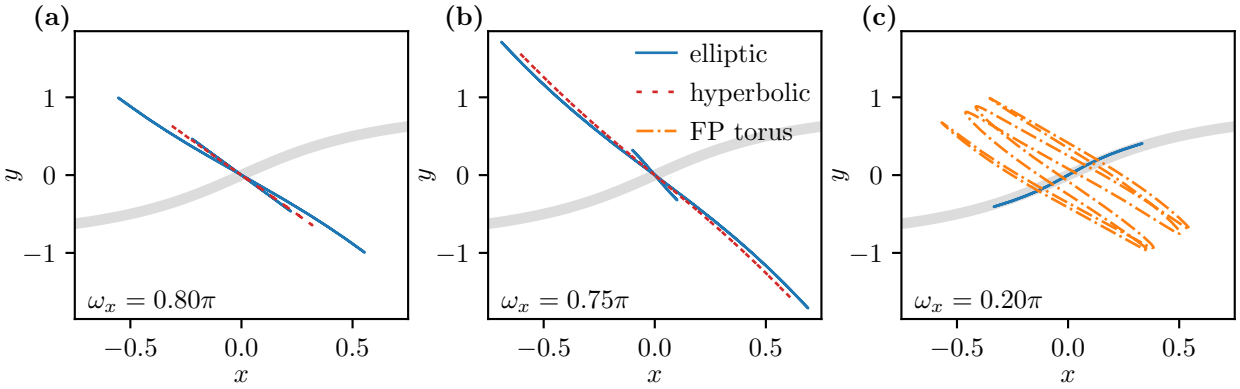


Fig. 5. Position (x, y) of periodic orbits on the NHIM for different frequencies ω_x. The driving amplitude is fixed at $\hat{x} = 0.4$. The minimum energy path is shown as a thick, light gray line. (a) With a frequency $\omega_x = 0.8\pi$ just below the bifurcation, all fixed point trajectories perform a single oscillation per period roughly orthogonal to the minimum energy path. (b) Decreasing the frequency to $\omega_x = 0.75\pi$ leads to the same configuration in principle, although with significant changes to the oscillation amplitudes. (c) With $\omega_x = 0.2\pi$ the situation changes fundamentally. The trajectory associated with the central elliptic fixed point now follows roughly the reaction coordinate approximated by the minimum energy path. In doing so, the trajectory always stays near the saddle point. Trajectories belonging to the fixed point torus, on the other hand, oscillate in direction of the orthogonal mode. Furthermore, these trajectories oscillate many times per driving period and fan out instead of following the same path back and forth. The legend in (b) is shared among all panels.

3.1.2. Trajectories in position space for different driving frequencies

The next step in the classification of the dynamics requires the characterization of the periodic trajectories associated with the fixed points found in Sec. 3.1.1.

Figure 5a shows the trajectories associated with the three fixed points in Fig. 4b just below the bifurcation. All three trajectories follow very similar paths roughly orthogonal to the minimum energy path given by the arctangent in Eq. (2.1). The elliptic and hyperbolic fixed points created in the bifurcation from Fig. 4a belong to trajectories oscillating in phase. By contrast, the trajectory associated with the second elliptic fixed point oscillates in antiphase with a higher amplitude. This is in accordance with its higher mean energy $\bar{E}_{\mathrm{tot}}$ as shown in Fig. 5a. The slight curvature of the trajectories is caused by the system's nonlinearity.

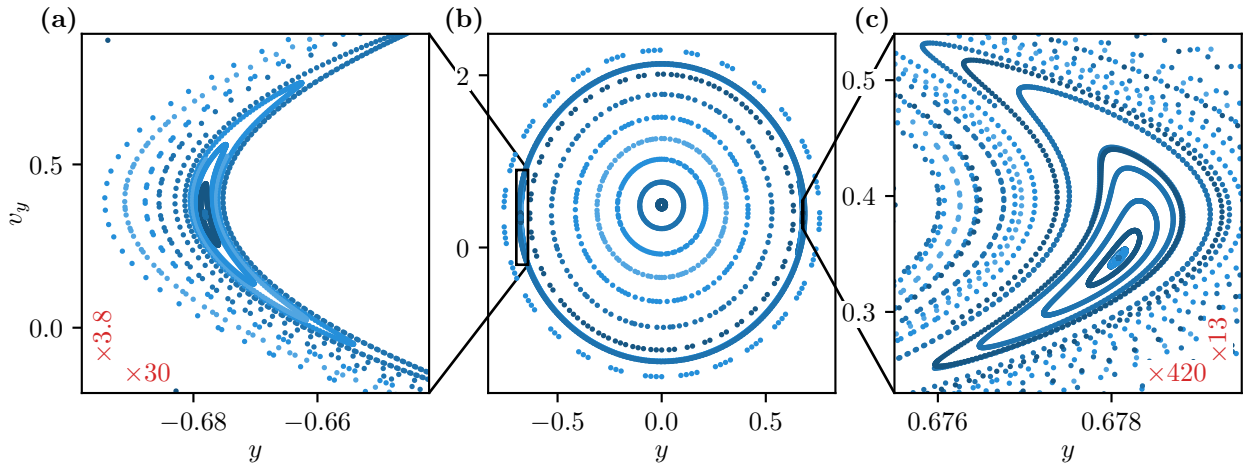


Fig. 6. Stroboscopic map of trajectories (PSOS) started at time $t_0 = 0$ for driving frequency $\omega_x = 0.55\pi$ and driving amplitude $\hat{x} = 0.4$. A color gradient is used to help distinguish neighboring trajectories. (b) From the overview an elliptic fixed point is clearly visible. (a) and (c) show magnified sections of (b) revealing two more elliptic fixed points. Different magnifications for the left/right-hand side are used since (b) is symmetric under reflection at $y = 0$. Labels in the bottom left/right corners indicate the approximate y and v_y zoom factors compared to (b).

The nonlinearity is also likely responsible for the bifurcation at $\omega_x \approx 0.802$: In the high energy limit $\bar{E}_{\text{tot}} \to \infty$, trajectories mostly see an effective potential of the form $V(x, y) = 2y^2$. This potential leads to an eigenfrequency of $\omega = 2 \approx 0.637\pi$ for the orthogonal mode y. For lower energies $\bar{E}_{\text{tot}}$, however, the barrier and the nonlinear coupling (through the arctangent) need to be taken into account. As a result, the direction of the orthogonal mode changes to roughly $y - x$ with an increased eigenfrequency. The system therefore supports a range of frequencies as a function of energy. Driving the system with a specific frequency ω_x within this range selects the corresponding trajectory and associated fixed point.

In Fig. 4a, two branches show a strong increase of the fixed point energies $\bar{E}_{\text{tot}}$ when the frequency ω_x is lowered, quickly rising beyond the limits of numerical feasibility. This diverging behavior can also be explained by the aforementioned mechanism since the approximation $V(x, y) = 2y^2$ is only valid for $\bar{E}_{\text{tot}} \to \infty$. The sensitivity of the oscillation amplitude is visible in the dramatic change in the amplitude of the periodic orbits in Figs. 5a and 5b resulting from the slight reduction in ω_x from 0.8π to 0.75π. The fact that the oscillation of the smaller amplitude orbit decreases between the cases in Figs. 5a and Figs. 5b can be attributed to its antiphase oscillation.

Upon lowering the frequency to $\omega_x = 0.2\pi$ (cf. Fig. 5c), only the antiphase fixed point remains. In contrast to Figs. 5a and 5b, its motion now oscillates in phase along the minimum energy path. In addition, a torus with infinitely many fixed points has emerged. A typical trajectory associated with one fixed point on the torus is shown in Fig. 5c. Compared to all the trajectories shown so far, it oscillates multiple times per period and fans out instead of remaining on a single periodic path. These fixed points can be attributed to a sign change in the torus's winding number.

3.2. Resonant tori

Changing the driving frequency to $\omega_x = 0.55\pi$ results in the occurrence of two elliptic fixed points with period $2T$. This can be observed in the PSOS by choosing a proper resolution, as shown in Fig. 6. Note that the stroboscopic map still records points every T units of time. The fixed point located at the center of the phase space (cf. Fig. 6b) is the elliptic fixed point that emerged from the saddle-node bifurcation in Fig. 4a.

The new fixed points with period $2T$ can be understood using the Poincaré–Birkhoff fixed point theorem [72, 73]. It allows the use of the PSOS to predict structural changes of resonant tori when the system is perturbed. Specifically, a change in the driving frequency can be seen in Fig. 6 as a perturbation which causes some of the tori with rational winding numbers to be destroyed. It results in an even number of fixed points, alternating between elliptic and hyperbolic ones. Increasing the

perturbation of such a system can also tear apart the tori in the vicinity of the $2T$ elliptic fixed points, forming new fixed points. Eventually, this leads to self-similar structures. In principle, one could expect to see such self-similar structures in Fig. 6 when further zooming the enlarged panels 6a and 6c. However, we did not continue such zooming here because resolution is limited by numerical precision.

4. CONCLUSION AND OUTLOOK

In this paper, we have investigated the constrained dynamics on the NHIM in a time-dependent two-dimensional system. Using Poincaré surfaces of section, we demonstrate the occurrence of structural changes of the dynamics, *viz.*, bifurcations of periodic TS trajectories when changing the amplitude and frequency of the external driving. In particular, periodic TS trajectories with the same period as the external driving but significantly different parameters such as mean energy compared to the ordinary TS trajectory can be created in a saddle-node bifurcation.

The model system investigated in this work, featuring a periodically driven rank-1-saddle, is paradigmatic of many chemical reactions in which the reaction takes place along a reaction path which is in turn affected by the mode to which it is most strongly coupled to. We characterized the dependence of the system's dynamics on the parameters of the periodic driving at the saddle i. e., through its frequency and amplitude. The dynamics of trajectories on the NHIM is unstable because of its proximity to the rank-1-saddle, but it can nevertheless be obtained numerically through the use of stabilizing techniques as shown here. The resulting dynamics was analyzed through stroboscopic maps, and observed to be regular for all parameter sets which have been investigated. At low driving frequencies of the saddle, a fixed point with a period twice that of the driving was observed. At higher frequencies, it was also possible to track the fixed points and observe the creation and annihilation of pairs of fixed points in saddle-node-bifurcations. The behavior of the periodic trajectories was also projected onto position space leading to the observation that the saddle frequency has a significant influence on the oscillation direction of the trajectories.

These results lead to a better understanding of the reaction dynamics of driven reactions. Changes in the parameters of the driving have a huge impact on the system's dynamics and have been seen here and recently [68] to lead to changes in mean energies and decay rates. Indeed, it suggests that one could control rate constants within a limited range by adjusting the driving of the system.

It remains to characterize the behavior of driven chemical reaction dynamics as a function of other system parameters, including the height and width of the saddle or the various parameters associated with the orthogonal mode. Changing these parameters could lead to further bifurcations, paving the way for the possible observation of a chaotic regime.

ACKNOWLEDGMENTS

We thank Tobias Mielich, Robin Bardakcioglu, and Matthias Feldmaier for fruitful discussions.

FUNDING

The German portion of this collaborative work was partially supported by the Deutsche Forschungsgemeinschaft (DFG) through Grant No. MA1639/14-1. The US portion was partially supported by the National Science Foundation (NSF) through Grant No. CHE 1700749. This collaboration has also benefited from support by the European Union's Horizon 2020 Research and Innovation Program under the Marie Skłodowska-Curie Grant Agreement No. 734557.

REFERENCES

1. K. S. Pitzer, F. T. Smith, and H. Eyring, *The Transition State*, Special Publ. (Chemical Society, London, 1962).
2. P. Pechukas, Annu. Rev. Phys. Chem. **32**, 159 (1981).
3. B. C. Garrett and D. G. Truhlar, J. Phys. Chem. **83**, 1052 (1979).
4. D. G. Truhlar, A. D. Issacson, and B. C. Garrett, *Theory of Chemical Reaction Dynamics* (CRC Press, Boca Raton, FL, 1985), vol. 4, pp. 65–137.
5. J. T. Hynes, Annu. Rev. Phys. Chem. **36**, 573 (1985).

6. B. J. Berne, M. Borkovec, and J. E. Straub, J. Phys. Chem. **92**, 3711 (1988).
7. A. Nitzan, Adv. Chem. Phys. **70**, 489 (1988).
8. P. Hänggi, P. Talkner, and M. Borkovec, Rev. Mod. Phys. **62**, 251 (1990), and references therein.
9. G. A. Natanson, B. C. Garrett, T. N. Truong, T. Joseph, and D. G. Truhlar, J. Chem. Phys. **94**, 7875 (1991).
10. D. G. Truhlar, B. C. Garrett, and S. J. Klippenstein, J. Phys. Chem. **100**, 12771 (1996).
11. D. G. Truhlar and B. C. Garrett, J. Phys. Chem. B **104**, 1069 (2000).
12. T. Komatsuzaki and R. S. Berry, Proc. Natl. Acad. Sci. U.S.A. **98**, 7666 (2001).
13. E. Pollak and P. Talkner, Chaos **15**, 026116 (2005).
14. H. Waalkens, R. Schubert, and S. Wiggins, Nonlinearity **21**, R1 (2008).
15. T. Bartsch, J. M. Moix, R. Hernandez, S. Kawai, and T. Uzer, Adv. Chem. Phys. **140**, 191 (2008).
16. S. Kawai and T. Komatsuzaki, Phys. Rev. Lett. **105**, 048304 (2010).
17. R. Hernandez, T. Bartsch, and T. Uzer, Chem. Phys. **370**, 270 (2010).
18. O. Sharia and G. Henkelman, New J. Phys. **18**, 013023 (2016).
19. C. Jaffé, D. Farrelly, and T. Uzer, Phys. Rev. Lett. **84**, 610 (2000).
20. G. Jacucci, M. Toller, G. DeLorenzi, and C. P. Flynn, Phys. Rev. Lett. **52**, 295 (1984).
21. T. Komatsuzaki and R. S. Berry, J. Chem. Phys. **110**, 9160 (1999).
22. T. Komatsuzaki and R. S. Berry, Adv. Chem. Phys. **123**, 79 (2002).
23. M. Toller, G. Jacucci, G. DeLorenzi, and C. P. Flynn, Phys. Rev. B **32**, 2082 (1985).
24. A. F. Voter, F. Montalenti, and T. C. Germann, Annu. Rev. Mater. Res. **32**, 321 (2002).
25. H. P. de Oliveira, A. M. Ozorio de Almeida, I. Damião Soares, and E. V. Tonini, Phys. Rev. D **65**, 083511/1 (2002).
26. C. Jaffé, S. D. Ross, M. W. Lo, J. Marsden, D. Farrelly, and T. Uzer, Phys. Rev. Lett. **89**, 011101 (2002).
27. H. Waalkens, A. Burbanks, and S. Wiggins, Mon. Not. R. Astron. Soc. **361**, 763 (2005).
28. C. Huepe, S. Métens, G. Dewel, P. Borckmans, and M. E. Brachet, Phys. Rev. Lett. **82**, 1616 (1999).
29. C. Huepe, L. S. Tuckerman, S. Métens, and M. E. Brachet, Phys. Rev. A **68**, 023609 (2003).
30. A. Junginger, J. Main, G. Wunner, and M. Dorwarth, J. Phys. A: Math. Theor. **45**, 155201 (2012).
31. A. Junginger, M. Dorwarth, J. Main, and G. Wunner, J. Phys. A: Math. Theor. **45**, 155202 (2012).
32. A. Junginger, M. Kreibich, J. Main, and G. Wunner, Phys. Rev. A **88**, 043617 (2013).
33. T. Bartsch, R. Hernandez, and T. Uzer, Phys. Rev. Lett. **95**, 058301 (2005).
34. T. Bartsch, T. Uzer, and R. Hernandez, J. Chem. Phys. **123**, 204102 (2005).
35. F. Revuelta, G. T. Craven, T. Bartsch, F. Borondo, R. M. Benito, and R. Hernandez, J. Chem. Phys. **147**, 074104 (2017).
36. C. Mendoza and A. M. Mancho, Phys. Rev. Lett. **105**, 038501 (2010).
37. A. M. Mancho, S. Wiggins, J. Curbelo, and C. Mendoza, Commun. Nonlinear Sci. Numer. Simul. **18**, 3530 (2013).
38. M. Feldmaier, A. Junginger, J. Main, G. Wunner, and R. Hernandez, Chem. Phys. Lett. **687**, 194 (2017).
39. M. Feldmaier, P. Schraft, R. Bardakcioglu, J. Reiff, M. Lober, M. Tschöpe, A. Junginger, J. Main, T. Bartsch, and R. Hernandez, J. Phys. Chem. B **123**, 2070 (2019).
40. R. Bardakcioglu, A. Junginger, M. Feldmaier, J. Main, and R. Hernandez, Phys. Rev. E **98**, 032204 (2018).
41. P. Talkner, E. Hershkovitz, E. Pollak, and P. Hänggi, Surf. Sci. **437**, 198 (1999).
42. G. E. Murgida, D. A. Wisniacki, P. I. Tamborenea, and F. Borondo, Chem. Phys. Lett. **496**, 356 (2010).
43. F. Revuelta, R. Chacón, and F. Borondo, Europhys. Lett. **110**, 40007 (2015).
44. G. E. Murgida, F. J. Arranz, and F. Borondo, J. Chem. Phys. **143**, 214305 (2015).
45. A. Shukla and S. Keshavamurthy, J. Phys. Chem. B **119**, 11326 (2015).
46. M. Feldmaier, J. Reiff, R. M. Benito, F. Borondo, J. Main, and R. Hernandez, J. Chem. Phys. **153**, 084115 (2020).
47. S. Wiggins, *Normally Hyperbolic Invariant Manifolds in Dynamical Systems* (Springer New York, New York, NY, 1994).
48. G. Haller, T. Uzer, J. Palacián, P. Yanguas, and C. Jaffé, Nonlinearity **24**, 527 (2011).
49. C.-B. Li, A. Shoujiguchi, M. Toda, and T. Komatsuzaki, Phys. Rev. Lett. **97**, 028302 (2006).
50. H. Teramoto, G. Haller, and T. Komatsuzaki, Chaos **23**, 043107 (2013).
51. P. Pechukas and E. Pollak, J. Chem. Phys. **67**, 5976 (1977).
52. E. Pollak and P. Pechukas, J. Chem. Phys. **69**, 1218 (1978).
53. E. Pollak, M. S. Child, and P. Pechukas, J. Chem. Phys. **72**, 1669 (1980).
54. C.-B. Li, M. Toda, and T. Komatsuzaki, J. Chem. Phys. **130**, 124116 (2009).
55. H. Teramoto, M. Toda, and T. Komatsuzaki, Phys. Rev. Lett. **106**, 054101 (2011).

56. H. Teramoto, M. Toda, and T. Komatsuzaki, Nonlinearity **28**, 2677 (2015).
57. H. Teramoto, M. Toda, M. Takahashi, H. Kono, and T. Komatsuzaki, Phys. Rev. Lett. **115**, 093003 (2015).
58. T. Bartsch, T. Uzer, J. M. Moix, and R. Hernandez, J. Chem. Phys. **124**, 244310 (2006).
59. S. Kawai and T. Komatsuzaki, J. Chem. Phys. **131**, 224505 (2009).
60. G. T. Craven, T. Bartsch, and R. Hernandez, Phys. Rev. E **89**, 040801(R) (2014).
61. G. T. Craven, T. Bartsch, and R. Hernandez, J. Chem. Phys. **141**, 041106 (2014).
62. G. T. Craven, T. Bartsch, and R. Hernandez, J. Chem. Phys. **142**, 074108 (2015).
63. A. Junginger and R. Hernandez, J. Phys. Chem. B **120**, 1720 (2016).
64. A. Junginger, G. T. Craven, T. Bartsch, F. Revuelta, F. Borondo, R. M. Benito, and R. Hernandez, Phys. Chem. Chem. Phys. **18**, 30270 (2016).
65. A. Junginger and R. Hernandez, Phys. Chem. Chem. Phys. **18**, 30282 (2016).
66. S. Kawai, H. Teramoto, C.-B. Li, T. Komatsuzaki, and M. Toda, Adv. Chem. Phys. **145**, 123 (2011).
67. M. Feldmaier, R. Bardakcioglu, J. Reiff, J. Main, and R. Hernandez, J. Chem. Phys. **151**, 244108 (2019).
68. M. Tschöpe, M. Feldmaier, J. Main, and R. Hernandez, Phys. Rev. E **101**, 022219 (2020).
69. J. Reiff, M. Feldmaier, J. Main, and R. Hernandez, submitted to Phys. Rev. E.
70. A. J. Lichtenberg and M. A. Liebermann, *Regular and Stochastic Motion* (Springer, New York, 1982).
71. P. Virtanen, R. Gommers, T. E. Oliphant, M. Haberland, T. Reddy, D. Cournapeau, E. Burovski, P. Peterson, W. Weckesser, J. Bright, et al., Nat. Methods **17**, 261 (2020).
72. S. Wimberger, *Nonlinear Dynamics and Quantum Chaos* (Springer International Publishing, Cham, 2014), URL `https://doi.org/10.1007/978-3-319-06343-0`.
73. H. Schuster and W. Just, *Deterministic Chaos* (Wiley-VCH, Weinheim, 2005), fourth edition ed.